

# Inkjet-Printed rGO/binary Metal Oxide Sensor for Predictive Gas Sensing in a Mixed Environment

Osarenkhoe Ogbeide, Garam Bae, Wenbei Yu, Ewan Morrin, Yungyu Song, Wooseok Song, Yu Li, Bao-Lian Su, Ki-Seok An, and Tawfique Hasan\*

Selectivity for specific analytes and high-temperature operation are key challenges for chemiresistive-type gas sensors. Complementary hybrid materials, such as reduced graphene oxide (rGO) decorated with metal oxides enables realization of room-temperature sensors with enhanced sensitivity. However, sensor training to identify target gases and accurate concentration measurement from gas mixtures still remain very challenging. This work proposes hybridization of rGO with  $\text{CuCoO}_x$  binary metal oxide as a sensing material. Highly stable, room-temperature  $\text{NO}_2$  sensors with a 50 ppb of detection limit is demonstrated using inkjet printing. A framework is then developed for machine-intelligent recognition with good visibility to identify specific gases and predict concentration under an interfering atmosphere from a single sensor. Using ten unique parameters extracted from the sensor response, the machine learning-based classifier provides a decision boundary with 98.1% accuracy, and is able to correctly predict previously unseen  $\text{NO}_2$  and humidity concentrations in an interfering environment. This approach enables implementation of an intelligent platform for printable, room-temperature gas sensors in a mixed environment irrespective of ambient humidity.

room-temperature gas sensors due to the synergistic effects of their properties; the low-dimensional, conductive nature of graphene; and highly catalytic reactivity at the localized heterojunctions of the BMOs.<sup>[1,2]</sup> Indeed, graphene is regarded as an excellent transducer platform and it sensitively reflects the electrical charge interaction that occurs at the interfaces between MOx and the analyte gas molecules.<sup>[3,4]</sup> This has been facilitated by the progress in hydrothermal synthesis of graphene and metal oxide nanoparticles and their functional inkjet printing,<sup>[5,6]</sup> enabling scalable manufacturing with high-precision and automated deposition of sensing layers for reliable device performance.<sup>[6–8]</sup>

However, despite intriguing properties of reduced graphene oxide (rGO)/MOx hybrid-based gas sensors, a vital prerequisite for their practical application remains elusive: lack of innovative strategies for implementation of intelligent gas sensors

## 1. Introduction

Graphene-based hybridization with binary metal oxides (BMOs) offers a great opportunity to enable highly sensitive and

sensors that are capable of identifying target gas species and their exact concentration under varying environments.<sup>[9–13]</sup> To minimize the effect of interfering gases on the response signal of sensing materials, a wide range of efforts via physicochemical approaches have been reported. These can be broadly classified into two groups: i) introduction of molecular sieves with functional porous nanomaterials, such as metal–organic frameworks, to prevent physical contact with interrupting gas molecules<sup>[14,15]</sup> and ii) surface functionalization with the incorporation of noble metal particles to maximize the chemical catalytic effect for the target gas species.<sup>[16,17]</sup> Nevertheless, those efforts have remained insufficient to overcome the fundamental limitation of distinguishing the sensor response to target gases in a mixed environment. Along these lines, an artificial intelligence-based statistical data analysis can be adopted to exploit the regularities and differences in sensor responses that are difficult for humans to perceive from a large amount of characteristic parameter data. In this context, by inferring from comparison of responses or electrical signals, machine learning (ML) based on statistical data processing has been widely used to offer insights into identifying multiple gases. However, these approaches only partially address the selectivity issues.<sup>[18–20]</sup> For integrated analysis of accurate gas classification and concentration regression, ML-supported predictive strategies based on observable visual information could offer a step change toward truly intelligent gas sensors.

O. Ogbeide, G. Bae, W. Yu, E. Morrin, Y. Song, T. Hasan  
Cambridge Graphene Centre  
University of Cambridge  
Cambridge CB3 0FA, UK  
E-mail: th270@cam.ac.uk

W. Yu, Y. Li, B.-L. Su  
State Key Laboratory of Advanced Technology for Materials  
Synthesis and Processing  
Wuhan University of Technology  
Wuhan, Hubei 430070, P. R. China

W. Song, K.-S. An  
Thin Film Materials Research Center  
Korea Research Institute of Chemical Technology (KRICT)  
141 Gajeong-ro, Yuseong-gu, Daejeon 34114, Republic of Korea

The ORCID identification number(s) for the author(s) of this article can be found under <https://doi.org/10.1002/adfm.202113348>.

© 2022 The Authors. Advanced Functional Materials published by Wiley-VCH GmbH. This is an open access article under the terms of the Creative Commons Attribution License, which permits use, distribution and reproduction in any medium, provided the original work is properly cited.

DOI: 10.1002/adfm.202113348

In a strong step toward this direction, we demonstrate a fully inkjet-printed rGO/CuCo<sub>x</sub> composite room-temperature gas sensor enabled by a principal component analysis (PCA)-assisted visualization platform. Our gas sensors based on graphene hybrids with BMOs show excellent gas sensing performance with high stability and reliability. To attain the capability of selective identification for specific gas under interference, we develop the ML model with both gas classification and regression onto 2D principal component (PC) space, with extraordinary prediction accuracy and readability by utilizing the pre-manipulated feature data from PCA.<sup>[20,21]</sup> The proposed strategy is the first demonstration, to the best of our knowledge, for the visualization of the data analysis process via a combination of regression surface onto decision map on to a PC space. Our findings can enable ML-based prediction and recognition with excellent visibility for low-power graphene-based sensors.

## 2. Results and Discussion

The synthesis of rGO/CuCo<sub>x</sub> sensing material is conducted using a hydrothermal process,<sup>[12,15]</sup> as detailed in the Experimental Section. After purification of this synthesized material, we formulate a stable, aggregation-free functional ink with isopropanol (IPA) and 2-butanol binary solvent carrier (Figure 1a). This enables inkjet printing with suppressed coffee-ring effect through Marangoni enhanced spreading.<sup>[8]</sup> A commercial silver nanoparticle (Ag NP)-based ink is adopted to print the interdigitated electrodes (IDEs) onto the porous PET substrate, followed by sintering. This choice of substrate allows well-defined inkjet printing of  $\approx 50 \mu\text{m}$  Ag IDEs with  $\approx 40 \mu\text{m}$  spacing without undesired electrical short circuits. Uniform inkjet printing of rGO/CuCo<sub>x</sub> fully covering the IDEs complete our fabrication of gas sensors (Figure 1b).

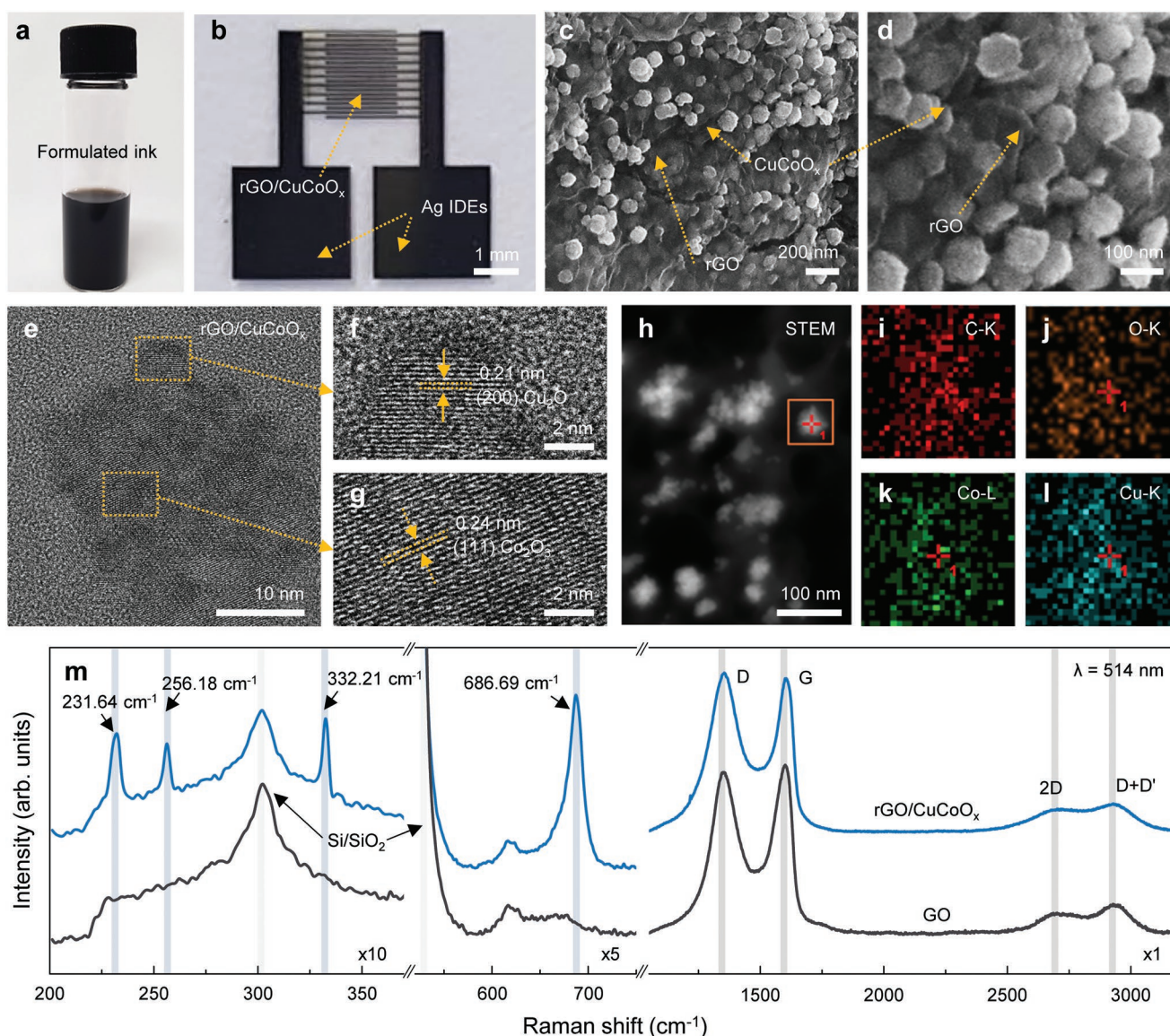


**Figure 1.** a) A photograph image of formulated rGO/CuCo<sub>x</sub> ink. b) Representative photograph image of fabricated gas sensor device with printed rGO/CuCo<sub>x</sub> sensing layer and Ag interdigitated electrodes (IDEs). c, d) FE-SEM images of rGO/CuCo<sub>x</sub> hybrid materials e) HR-TEM images of rGO/CuCo<sub>x</sub> and f, g) its enlarged images. h) STEM image of rGO/CuCo<sub>x</sub> composites. EDS elemental maps of i) C, j) O, k) Co, and l) Cu for rGO/CuCo<sub>x</sub>. m) Raman spectra for rGO/CuCo<sub>x</sub> (blue) and GO (black).

To explore structural characteristics of our synthesized rGO/CuCoO<sub>x</sub> hybrid sensing materials, we carry out field emission scanning electron microscopy (FE-SEM) (Figure 1c,d). The size of the CuCoO<sub>x</sub> nanoclusters in SEM images (Figure 1c,d) is estimated as ≈100 nm due to densely packed clusters of the nano particles. However, the CuCoO<sub>x</sub> monodispersed nanoparticles from these same samples, as prepared for transmission electron microscopy (TEM) analysis, shows uniformly grown 30 nm diameter particles over the entire surface of the rGO nanosheets (Figure S1, Supporting Information). Such direct synthesis enables robust electrical path between the BMO and the rGO scaffold.<sup>[22]</sup> To better understand the structural features, HR-TEM images of a clustered nanoparticle of rGO/CuCoO<sub>x</sub> are closely studied (Figure 1e–g). The long-range order lattice fringes with an interplanar spacing of 0.21 nm corresponds to the (200) planes of Cu<sub>2</sub>O and a lattice spacing of 0.24 nm matches with the (111) plane of Co<sub>2</sub>O<sub>3</sub>, confirming the coexistence of copper- and cobalt-oxide phases in the CuCoO<sub>x</sub> clustered nanoparticles.<sup>[23]</sup> To further validate the spatial distribution of the constituent atomic elements, we conduct energy-dispersive X-ray spectroscopy (EDS) elemental mapping coupled with STEM observations. Figure 1h–l presents the cross-sectional STEM and EDS elemental mapping images for rGO/CuCoO<sub>x</sub> nanoparticles, showing the uniform spatial distributions of the mixed elements (C, O, Co, and Cu) on larger scales after the rational hybridization. Raman spectroscopy of the rGO/CuCoO<sub>x</sub> hybrids is also carried out to further elucidate the structural and chemical evolution (Figure 1m). For the pristine GO, two strong characteristic peaks are observed at ≈1370 and ≈1618 cm<sup>-1</sup>, corresponding to the D-, G-band of graphene oxide, respectively. The intensity ratio of the Raman D-band to G-band ( $I_D/I_G$ ) for graphene oxide is 0.96. In the Raman spectrum of rGO/CuCoO<sub>x</sub> hybrids, the fingerprints of graphene oxide are clearly ascertained with slight increase of the  $I_D/I_G$ . This can be referred to the increase in edge of the *sp*<sup>2</sup> domains under the reduction process.<sup>[24]</sup> Additionally, the four pronounced characteristic peaks for CuCoO<sub>x</sub> synthesized from the rGO/CuCoO<sub>x</sub> hybrids are unequivocally ascertained at 231.64, 256.18, 332.21, and 686.69 cm<sup>-1</sup> and are in good agreement with previous reports.<sup>[25–27]</sup> From the above discussions, we conclude that optimized hydrothermal growth and binary solvent formulation for inkjet printing enables fabrication of rGO/CuCoO<sub>x</sub> gas sensors with high material uniformity.

Both the copper and cobalt oxides are representative p-type metal oxide semiconductors. For p-type metal oxides, the gas sensing mechanism can be elucidated by the competition between the parallel electrical path of resistive core and hole accumulated shell, which arise from electrical interaction between the target gas molecules and the adsorbed oxygen ions on the surface.<sup>[28,29]</sup> Upon exposure to the oxidizing NO<sub>2</sub> molecules, electron transfer from the sensing material into the adsorbed NO<sub>2</sub> molecules leads to increase in hole doping at the surface of oxide domains. This subsequently influences the enhancement of electrical conductivity due to the increase of the majority charge carriers. As a metallic inter-bridging network, rGO is considered a transducer that converts chemical interactions and electronic structure evolution between metal oxide nanoparticles and target gases into discernable electrical signals. The electron transfer from metal oxides to the adsorbed

oxidizing gas, such as NO<sub>2</sub>, causes charge compensation from rGO, resulting in more p-doping of rGO (i.e., increase in current) that are innately p-type in nature due to the oxygen-functional groups at the surface.<sup>[30]</sup>

Figure 2a shows the response for the rGO/CuCoO<sub>x</sub>-based resistive gas sensors with varied NO<sub>2</sub> gas concentrations. The gas response (*S*) can be defined as:  $S (\%) = (I_{\text{gas}} - I_0)/I_0$ , where  $I_{\text{gas}}$  is the current when exposed to a target gas and  $I_0$  is the current at the initial stage. The gas sensors are operated at room temperature. All the devices reveal abrupt response modulation under gas injection with altered gas concentrations. The gas response of the rGO/CuCoO<sub>x</sub>-based gas sensors are 3.93%, 6.22%, 11.48%, 16.64%, 24.25%, and 64.76%, corresponding to 50, 200, 400, 600, 800, and 1000 ppb of NO<sub>2</sub> concentration, respectively (Figure 2b). The cyclic gas response of the rGO/CuCoO<sub>x</sub>-based gas sensors under a periodic injection of 50 ppb NO<sub>2</sub> is shown in Figure 2c, further ascertaining the repeatability and reliability of the sensor response at low gas concentration, with 2.396% of average response and 0.28% standard deviation.

We calculate the signal-to-noise ratio (SNR) extracted from Figure 2c, defined as  $\mu_S/\sigma_N$ , where  $\mu_S$  is the mean value of the signal, and  $\sigma_N$  is the standard deviation of the noise in the baseline. The measured value for  $\sigma_N$  is 0.01129%, while the average of gas response under 50 ppb NO<sub>2</sub> is 2.396%. Therefore, the SNR value can be calculated as 212.2. This is reasonable compared to the commonly assumed 3.0 of SNR for commercial devices, regarded as the requirement for the detection limit according to IUPAC definition.<sup>[31,32]</sup> Consequently, 50 ppb for NO<sub>2</sub> can be regarded as the limit of detection of rGO/CuCoO<sub>x</sub>-based gas sensor. We also compare the gas sensing performance of pure rGO and rGO/CuCoO<sub>x</sub> to confirm that the enhancement in response comes from the hybrid material, and not from pure rGO (Figure S2, Supporting Information). Indeed, compared to pure rGO, rGO/CuCoO<sub>x</sub> has four times the response to low NO<sub>2</sub> concentration (250 ppb) and is drastically less noisy. We further note that pure CuCoO<sub>x</sub>-based sensor exhibits resistance values beyond the measurement range at the same operating condition, likely due to the discretely clustered NPs.

We also explore the response of the sensor under a range of gas species (250 ppb of NH<sub>3</sub>, mixtures of 250 ppb NO<sub>2</sub> with 250 ppb NH<sub>3</sub>, NO<sub>2</sub> [250 ppb] under humid air [10% and 20% of relative humidity (RH)], and pure humid air [10%, 20%, and 30% of RH]) to evaluate the selectivity of the sensor (Figure 2d and Figure S3, Supporting Information). The resulting response of the sensors are 0.28% (250 ppb of NH<sub>3</sub>), 3.53% (mixtures of 250 ppb NO<sub>2</sub> with 250 ppb NH<sub>3</sub>), 9.41% (250 ppb NO<sub>2</sub> under 10% of RH), 13.16% (250 ppb NO<sub>2</sub> under 20% of RH), 9.68% (10% of RH), 11.03% (20% of RH), and 14.97% (30% of RH). These results are summarized in Figure 2e with a scatter response plot for NO<sub>2</sub>. In general, the gas response depends on the combination of target-gas selectivity and its concentration. This indicates that the response between a low-concentration gas with high reactivity and a high-concentration gas with relatively low reactivity might be indistinguishable should the response curves look broadly similar. Meanwhile, in Figure 2e, the response 250 ppb of NO<sub>2</sub> under humid air (10% of RH) can be expected to be similar to the response for that of the 400 ppb NO<sub>2</sub> concentration (other similar responses: 250 ppb NO<sub>2</sub> under 10% humidity: 9.41%, 200 ppb NO<sub>2</sub>: 6.22%, 400 ppb NO<sub>2</sub>:

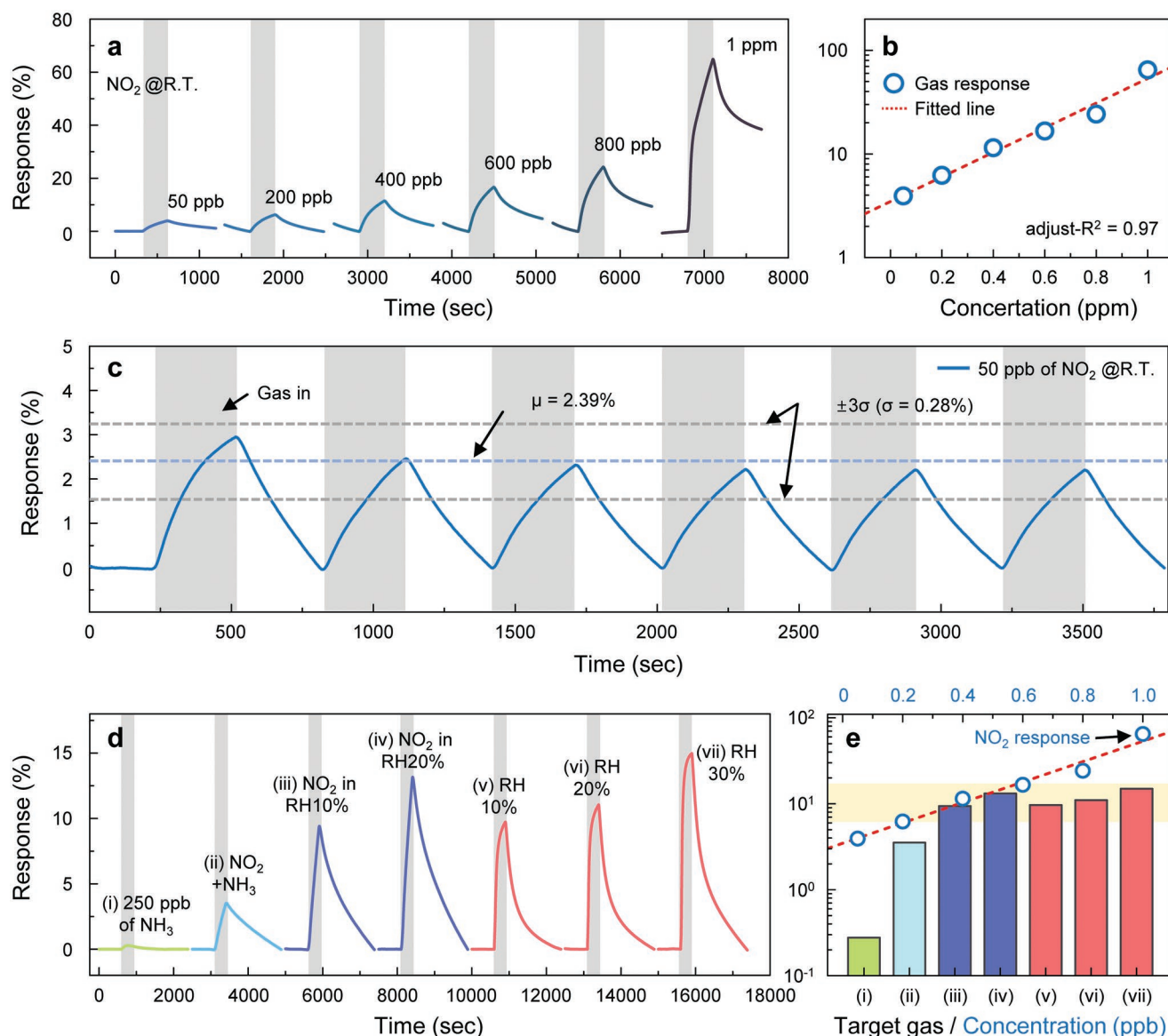


**Figure 2.** Gas sensing characteristics of the rGO/CuCoO<sub>x</sub> sensors. All measurements are carried out at room temperature. a) Dynamic gas response of rGO/CuCoO<sub>x</sub> gas sensors for varied NO<sub>2</sub> concentration (50 ppb to 1 ppm). b) A summarized plot of gas responses for NO<sub>2</sub>. c) Parts-per-billion-level (50 ppb) NO<sub>2</sub> sensing performance of rGO/CuCoO<sub>x</sub>-based sensors. d) The gas response of the rGO/CuCoO<sub>x</sub> sensors with the injection of 250 ppb of NH<sub>3</sub>: green, mixtures of 250 ppb NO<sub>2</sub> with 250 ppb NH<sub>3</sub>: sky blue, NO<sub>2</sub> (250 ppb) under humid air (10% and 20% of RH): purple blue, and humid air (10, 20, and 30% of RH): coral. e) A summarized plot of extracted gas response of the rGO/CuCoO<sub>x</sub>-based gas sensor for the various types of gas components and a stacked scatter plot of NO<sub>2</sub> gas response as a function of the concentration (top x axis).

11.48%). In addition, it is virtually impossible to classify the specific target gas between pure NO<sub>2</sub> and NO<sub>2</sub> in humid air by simply scoring the response values. This means that a comprehensive analysis based on data statistical process, such as PCA, ML-based classification, and regression, is further needed for gas recognition and concentration estimation.

**Figure 3a** shows a schematic illustration of the general process to demonstrate the PCA-driven gas recognition. First, we collect the sensor response for several types of gas species with varied concentration from Figure 2 and Figure S3, Supporting Information. The dynamic gas response curve corroborates a gas injection-dependent variation in electrical

signal. Also, the response curve can further suggest several additional features, reflecting the characteristics of the curves from the fitting parameters. Since two classes of a dataset consisting of labeled data (or answer data) and feature data are needed for utilizing the ML method, we rationally assign the class of target gas and its concentration as the labeled data. For the ML feature data, we assign the 2D scatters coordinated in a space of PCA, which is reduced from the ten extracted parameters from the response curves. Finally, we implement the PCA features to classify target gas and predict their concentration via PCA-assisted machine learning, which is a hybridized technique followed by the projection of the

discrete regression 3D surface on to a 2D map of classification in the space of PCA. To acquire the features for PCA, ten parameters are extracted from the dynamic response curve via exponential curve fitting, as shown in Figure S4, Supporting Information. The response curve can be regarded as the combination of two different curves in the region for gas response and gas recovery. Consequently, the individual curve for both response and recovery curves can be fitted by exponential growth (or decay) function, defined as

$$\text{Fitting curve} = \gamma_{\text{rsp/rec}} + C_{\text{rsp/rec}} \exp(-t/\tau_{\text{rsp/rec}}) \quad (1)$$

where  $\gamma$  is the offset,  $C$  is the fitting constant, and  $\tau$  the time constant. In addition, the features include maximum response value ( $S_{\text{max}}$ ), response time ( $T_{\text{rsp}}$ ), and integrated area under both response and recovery curves ( $A_{\text{rsp}}$  and  $A_{\text{rec}}$ ). Figure 3b shows a parallel coordinate plot of ten extracted parameters from all gas response measurements in Figure 2 and Figure S3, Supporting Information for NO<sub>2</sub>, humid air, NH<sub>3</sub>, NO<sub>2</sub> under humid air, and a mixture of NO<sub>2</sub> and NH<sub>3</sub> gases with varying concentrations. Each line on the parallel coordinate plot corresponds to a single point in the multi-dimensional parameter space, with lines connecting the values for each parameter on their respective (parallel) axes. This further provides a useful visual indication of clustering at the specific parameters in which the measurement of the gas response is converged. For example, it can be readily ascertained that groups of NO<sub>2</sub>-related gas converge near  $T_{\text{rsp}} = 230$  to form a cluster and are distinguished from that of the NH<sub>3</sub> and humid air. This indicates the possibility for efficient PCA-assisted clustering by using the extracted parameters.

To further corroborate the validity of those extracted parameters, we visualize the data points in the 3D space with the fitting parameters for response curve ( $\gamma_{\text{rsp}}$ ,  $C_{\text{rsp}}$ ,  $\tau_{\text{rsp}}$ ) in Figure S5, Supporting Information. Figure S5a, Supporting Information shows a 3D scatter plot of the fitting parameters  $\gamma_{\text{rsp}}$ ,  $C_{\text{rsp}}$ , and  $\tau_{\text{rsp}}$ . Their 2D projection plots are shown in Figure S5b,c, Supporting Information. It can be clearly manifested that a combination of  $\gamma_{\text{rsp}}$  and  $C_{\text{rsp}}$  enables the formation of three main clusters for NO<sub>2</sub>-related groups, NH<sub>3</sub>, and humid air, while the specific class for NO<sub>2</sub>-related groups can be further classified as the following three groups: pure NO<sub>2</sub>, NO<sub>2</sub> under humid air, and mixture of NO<sub>2</sub> and NH<sub>3</sub> in a space of  $\gamma_{\text{rsp}}$  and  $\tau_{\text{rsp}}$ . Based on these salient features, we can conclude that the extracted parameters from the gas dynamic response curves are able to facilitate clustering of the target gas and visualization of the classification decision boundary through the PCA-assisted machine learning; see Note 1, Supporting Information. This is because the parameters strongly reflect the characteristics in the response behavior of rGO/CuCoO<sub>x</sub>-based gas sensor for the target gases.

To capture the clustering features of the target gas, a PCA is performed using the ten extracted features. PCA is an orthogonal linear transformation that maps data to a new coordinate basis via a scalar projection, which serves as a dimension reduction technique to keep the essence of the data while providing plottable axes through the first two (or three) PCs.<sup>[33,34]</sup> For better visualization, we reduce the multi-dimensional dataset of the extracted parameters into 2D space (PC1, PC2). Figure 3c shows the resulting parameters of PCA including

the variance of the two PCs (PC1, PC2) and the loading scores of the extracted parameters on to the main principal components. The total variance from PC1 (75%) and PC2 (10%) is around 85%, and therefore, these components contain significant information from the extracted parameters and are a good reflection of the overall data. The right panel of Figure 3c illustrates the loading scores for each extracted parameter. A combination of the loading scores for principal components can form a vector, representing their influence on each of the principal components, as depicted by the gray arrows in Figure 3d. Furthermore, the angles between these vectors indicate their correlations to each other. Figure 3d is PCA scatter plot for five different types of target gas. Two distinctive features can be readily discerned. i) The three parameters from exponential fitting in the response region can be regarded as key identifier, which further signals that gas adsorption behavior is crucial for gas recognition. ii) Clear separation between the clusters representing individual gases with no overlap and a recognizable trend of concentration allows the identification of all analytes. This further indicates that PCA can be an adequate solution to reduce mass data into two meaningful principal components for the ML dataset.

To corroborate a scheme to discriminate the target gas among the five different groups, we employ supervised ML approach by using the extracted PCs as the feature data of ML. The classification is evaluated with common training algorithms including decision tree, linear discriminant, Naïve Bayes, support vector machine,  $k$ -nearest neighbor (kNN), ensemble bagged trees, and neural network with  $k$ -fold validation method ( $k = 5$ ), as depicted in Figure S6, Supporting Information.<sup>[35–37]</sup> The kNN is selected for classification as no assumption is required for its decision boundary. Figure 4a shows PCA-assisted ML results for decision map of five different groups by applying kNN model, which afford clear distinguishable boundary for NO<sub>2</sub> (orange), humid air (blue), NH<sub>3</sub> (salmon), NO<sub>2</sub> under humid air (purple), and a mixture of NO<sub>2</sub> and NH<sub>3</sub> (green). Figure 4b is a confusion matrix of five different target gases from the classification results of the kNN, showing 98.1% of prediction accuracy. Consequently, this is able to express the decision boundary map as a function of 2D PC coordinates with excellent visibility and prediction accuracy of the training model. Figure S7, Supporting Information shows the classification boundary map with varied training models, strongly reflecting the characteristics of the classifiers. From these results, it is worth noting that clear visual information can be provided by reducing dimensionality from multi-dimensional parameters to PC characteristics. Figure S8, Supporting Information represents the confusion matrix with the varied classifiers by using the original ten extracted features. The accuracy of training models is summarized in Figure S9, Supporting Information. We observe that there is no marked decrease in accuracy due to the limited number of feature data. This indicates that the PCs strongly reflect and conserve the information of the original ten extracted parameters.

To establish the training model for predicting the gas concentration, two regression models are trained for pristine NO<sub>2</sub> and relative humidity without data for intermediate gas concentration using a linear regression from the sklearn machine learning library. To evaluate the performance of the training

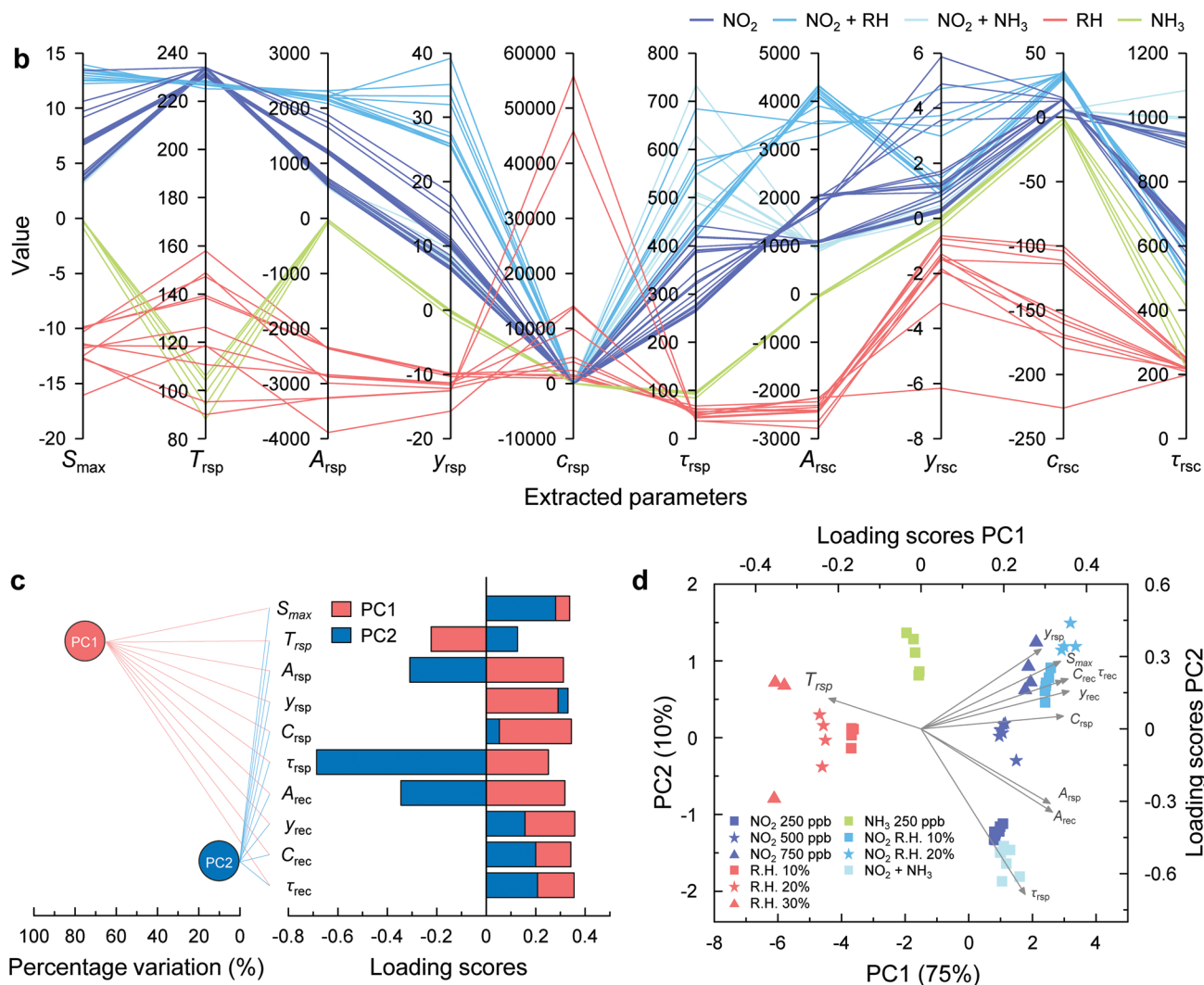
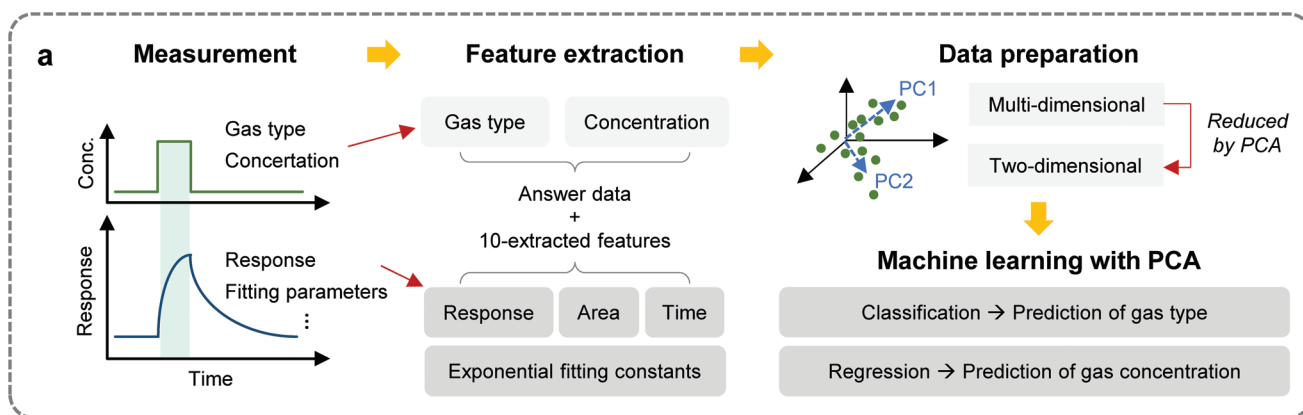


**Figure 3.** a) Schematic illustration of the data preparation for principal component analysis (PCA)-assisted classification. b) Parallel coordinate plot of ten extracted parameters from all gas response measurement: NO<sub>2</sub>-related group (navy: NO<sub>2</sub>, sky blue: NO<sub>2</sub> under humid air, cyan: mixture of NO<sub>2</sub> and NH<sub>3</sub>), humid air (coral), and NH<sub>3</sub> (green). c) Loading score of principal components for the ten extracted parameters. d) PCA scatter plot for five different types of target gas (NO<sub>2</sub>, humid air, NH<sub>3</sub>, NO<sub>2</sub> under humid air, and a mixture of NO<sub>2</sub> and NH<sub>3</sub>).

model, we carefully divide the dataset into two categories for training and validation (untrained). To predict the intermediate

concentrations, higher and lower concentrations are only utilized for the training model; meanwhile, the regression

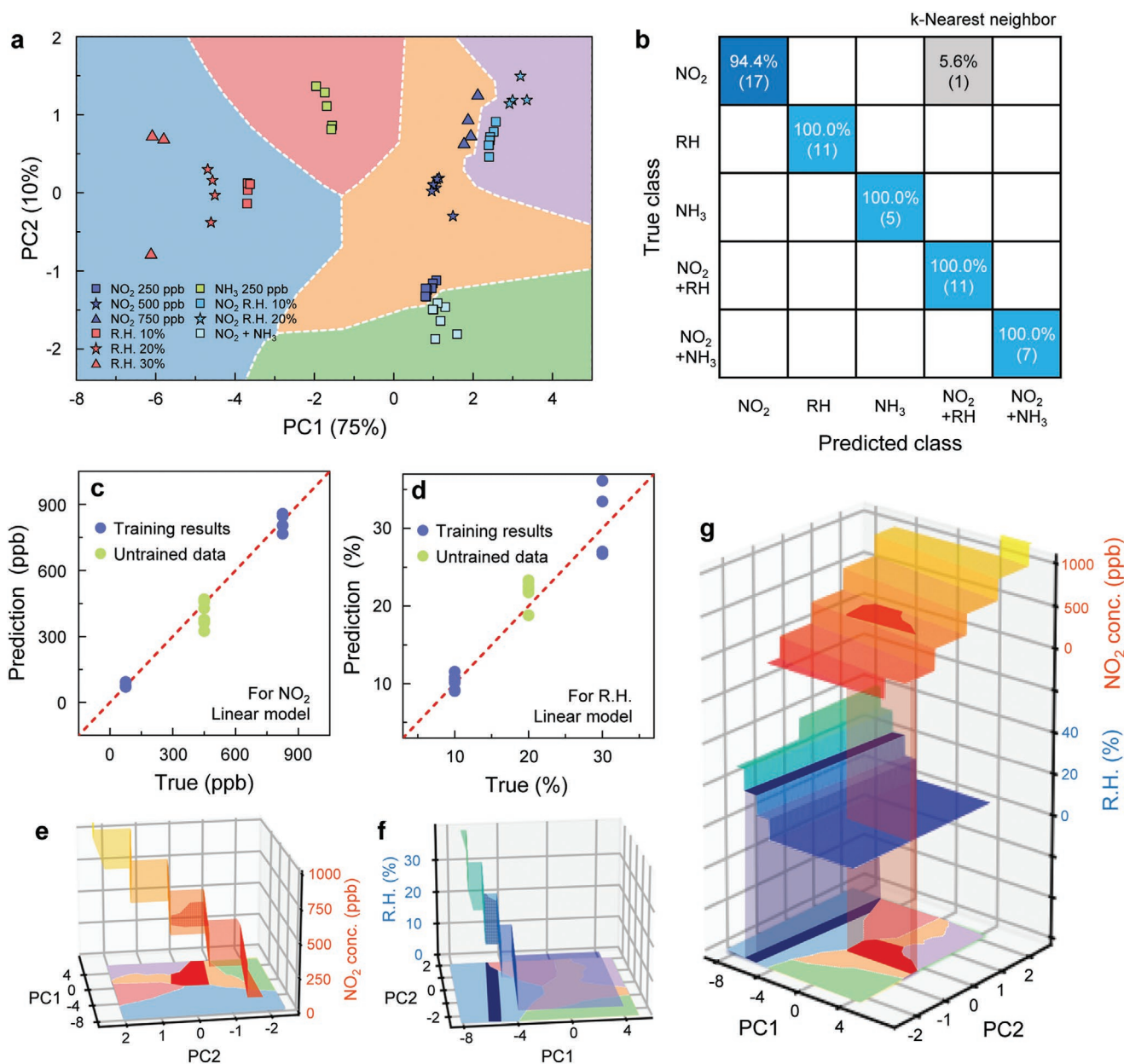


**Figure 4.** PCA-assisted machine learning (ML) results for classification and regression. a) Decision map of five different groups (NO<sub>2</sub>, humid air, NH<sub>3</sub>, NO<sub>2</sub> under humid air, and mixture of NO<sub>2</sub> and NH<sub>3</sub>) classified by applying a k-nearest neighbor (kNN) of ML model with k-fold validation (k = 5). b) Confusion matrix of five different target gases from the classification results by kNN. Relationships of predicted gas concentration versus real gas concentration for c) NO<sub>2</sub> and d) relative humidity (RH) Regression surface of the predicted concentration in PCs spaces for e) NO<sub>2</sub> and f) RH, and g) those of stacked plots with classification results.

models are not trained on any NO<sub>2</sub> at 500 ppb points or RH at 20% points. Consequently, we are able to use the untrained dataset to verify the validity of the predicted concentration data the model has not previously seen. In addition, we further optimize the training model to return the predefined discrete prediction levels instead of a linear prediction surface consistent with the mean of a probability distribution. For this, we select 250 ppb and 10% of concentration resolution for the NO<sub>2</sub> and RH steps, respectively. The prediction results for NO<sub>2</sub> and RH concentration are displayed in Figure 4c,d. The accuracy ( $R^2$ ) can be calculated using the residual scatter from the fitting line (red dashed line) as follows:

$$\text{Accuracy}(R^2, \%) = 1 - \frac{\sum (y - p)^2}{\sum (y - \bar{y})^2} \quad (2)$$

where  $y$  is the real value,  $p$  is the predicted value, and  $\bar{y}$  is the mean of the real value at the specified corresponding gas concentration. Then,  $y - p$  can be described as a residual scatter from the prediction of the real value through the machine learning results. Additionally,  $y - \bar{y}$  is the total variance. In general, because a higher  $R^2$  leads to a well-fitted model compared with the real values, the accuracy of the training model can be estimated using the  $R^2$  value. The ML results exhibit a high-scored accuracy of 97.12% for NO<sub>2</sub> and 88.5% for RH.

Figure 4e,f shows the regression surface of the predicted concentration with the predefined discrete resolution in PC spaces for NO<sub>2</sub> and RH, optimized from the established model in Figure 4c,d. Finally, the regression surface of predicted concentration can be projected down to 2D PC space to view the original classifier decision regions, as displayed in Figure 4g. The surface corresponding to 500 ppb of NO<sub>2</sub> is projected and represented by the red strip inside the NO<sub>2</sub> decision boundary of the classifier, exactly matching the real dataset that is not included to train the regression model. Likewise, the corresponding region for the 20% RH prediction surface is shaded in the blue strip. To further validate the selectivity among the other oxidizing gas species, the decision boundary of three different oxidizing gases, such as NO<sub>2</sub>, humid air, and CO<sub>2</sub>, are plotted onto the 2D PC space classified by adopting kNN of classifier with *k*-fold validation (*k* = 5), as displayed in Figure S10, Supporting Information. It can be readily discerned that three different gas species, NO<sub>2</sub>, humid air (RH), and CO<sub>2</sub> at 0.5 million ppm, are independently clustered and clearly separated. From these results, we can conclude that our PCA-based pretreatment offer notable visualization aid on to the reduced PC dimension space through classification of target gas and regression for its concentration, expanding available techniques to analyze sensing through ML-based recognition.

### 3. Conclusion

In summary, we propose a new strategy for a fully inkjet-printed graphene-BMO composite room-temperature gas sensor for predictive sensing under mixed environments. We systemically optimize and characterize the synthesized rGO/CuCoO<sub>x</sub> material, showing tightly packed clusters of Cu<sub>2</sub>O and Co<sub>2</sub>O<sub>3</sub> uniformly distributed over rGO. Using a binary solvent-based ink of this material for uniform printing, we demonstrate highly stable, sensitive, room-temperature NO<sub>2</sub> sensors with a 50 ppb detection limit. We additionally develop a framework for machine-intelligent recognition using a single rGO/CuCoO<sub>x</sub>-based sensor, showing extraordinary accuracy for identifying specific gases and predicting their concentration under an interfering atmosphere. The classifier allows a clearly distinguishable decision boundary map with 98.1% accuracy. In addition, our proposed regression model is able to predict untrained NO<sub>2</sub> and humidity concentration correctly. Our findings offer a robust solution for room-temperature gas detection in a mixed environment using a single sensor irrespective of ambient humidity.

### 4. Experimental Section

**Ink Formulation:** The rGO/CuCoO<sub>x</sub> hybrid materials were synthesized by following the one-pot hydrothermal process.<sup>[12,15]</sup> First, to secure a well-dispersed graphene oxide (GO) solution, 23 mg of GO powder was dispersed in 22 mL of deionized (DI) water and magnetically stirred for 30 min, then sequentially sonicated for 1 h. Next, 2 mL of ammonium hydroxide (NH<sub>4</sub>OH) was added to the GO solution and sonicated for another 1 h. Subsequently, 42.5 mg of sodium nitrate (NaNO<sub>3</sub>), 29.2 mg of cobalt nitrate (Co(NO<sub>3</sub>)<sub>2</sub>), and 14.7 mg of copper nitrate (Cu(NO<sub>3</sub>)<sub>2</sub>) were added and the mixture was stirred continuously for 3 h. The combined reagents were then transferred to a hydrothermal autoclave reactor and heated at 180 °C for 12 h. The sample was allowed to cool and vacuum filtrated using a

hydrophobic polytetrafluoroethylene (PTFE) membrane filter with 0.22 μm pore size. Filtration was repeated three times, rinsing the sample with DI water each time; the filtered sample was then dried in an oven at 60 °C. The dried CuCoO<sub>x</sub> decorated rGO flakes were scraped off the filter paper into a vial containing a 9:1 binary solvent mixture of IPA and 2-butanol and sonicated for 30 min. After the solvent exchange process, the sample was centrifuged at 1000 rpm for 10 min. The top 70% of the supernatant, without any visible aggregation, was collected for inkjet printing.

**Inkjet Printing and Characterizations:** The rGO/CuCoO<sub>x</sub> composited gas sensors were fabricated by inkjet printing (Dimatix Materials Printer DMP-2831, Fujifilm) on a porous polyethylene terephthalate (PET, Novacentrix) substrate. Note that the PET substrate was used to provide a lightweight and thin sensing platform rather than flexibility of the sensors during operation. For printing, the ink cartridge (Dimatix DMC-11610 Fujifilm) was adopted with a jetting nozzle diameter of 22 μm. To acquire the best sensing characteristics, the IDEs structure was optimized by considering the configuration of the electrodes, electrode spacing, and sensor geometry.<sup>[38–40]</sup> A commercial Ag NP dispersion (30–35 wt.% in triethylene glycol monomethyl ether, Sigma-Aldrich) was used to print the IDEs with 50 μm finger width and 42 μm gap. The ink cartridge containing the Ag NPs dispersion and printing stage were kept at 40 and 60 °C, respectively. Once the IDEs with Ag NPs on the porous PET substrate were sintered at 100 °C for 30 min, the rGO/CuCoO<sub>x</sub> ink is inkjet printed on the desired sensing area with heating 60 °C of the print stage. Ten print passes were used as the optimum deposition condition. To characterize the synthesized rGO/CuCoO<sub>x</sub> hybrid materials, comprehensive microscopic (scanning electron microscopy, SEM: Magellan 400L, high-resolution transmittance electron microscopy, HRTEM: JEOL 4000k) and spectroscopy analysis (Raman: Renishaw RM100) were performed.

**Gas Characterization:** Gas sensing measurements were carried out in a Kenosistec Gas Characterization System. All measurements were carried out at room temperature and 1 atm with 1 V of applied voltage. The concentration of target gas was carefully manipulated by regulating the ratio of the target gas to base gas with 500 sccm of total gas flow. A standardized pretreatment process was employed to ensure consistency of gas response and to reduce the environmental perturbations, as sequentially followed, i) vacuuming under a low 10<sup>-2</sup> torr, ii) heating up to 60 °C for 10 min, and iii) exposing to dry air for 40 min. The RH level of the experiment environment was controlled by balancing dry air with appropriate proportion of humid air, where humid air was produced by passing through a water bubbler.

**Data Processing:** To process the data analysis, ten features from the dynamic response curves were first extracted. Then, the PCA was employed to reduce multi-dimensional parameters into a 2D PCA space, which offered a benefit for visualization of the classification and regression results. MATLAB, Python, and Origin were used for signal processing, feature extraction, data classification, and visualization.

### Supporting Information

Supporting Information is available from the Wiley Online Library or from the author.

### Acknowledgements

The authors would like to acknowledge funding from the Engineering and Physical Sciences Research Council (EP/L016087/1) and Alphasense Limited in United Kingdom.

### Conflict of Interest

The authors declare no conflict of interest.

## Author Contributions

O.O., G.B., and W.Y. contributed equally to this work. The manuscript was written through contributions of all authors.

## Data Availability Statement

The data that support the findings of this study are available from the corresponding author upon reasonable request.

## Keywords

gas prediction, gas sensors, graphene, inkjet printing, machine learning, metal oxide, principal component analysis

Received: December 29, 2021

Revised: March 4, 2022

Published online:

- 
- [1] S. G. Chatterjee, S. Chatterjee, A. K. Ray, A. K. Chakraborty, *Sens. Actuators, B* **2015**, *11*, 1170.
- [2] T. Salehi, A. Taherizadeh, A. Bahrami, A. Allafchian, V. Ghafarinia, *Adv. Eng. Mater.* **2020**, *22*, 2000005.
- [3] E. Singh, M. Meyyappan, H. S. Nalwa, *ACS Appl. Mater. Interfaces* **2017**, *9*, 34544.
- [4] Z. Meng, R. M. Stolz, L. Mendecki, K. A. Mirica, *Chem. Rev.* **2019**, *119*, 478.
- [5] T. C. Wu, A. de Luca, Q. Zhong, X. Zhu, O. Ogbeide, D. S. Um, G. Hu, T. Albrow-Owen, F. Udrea, T. Hasan, *npj 2D Mater. Appl.* **2019**, *3*, 42.
- [6] J. Dai, O. Ogbeide, N. Macadam, Q. Sun, W. Yu, Y. Li, B. L. Su, T. Hasan, X. Huang, W. Huang, *Chem. Soc. Rev.* **2020**, *49*, 1756.
- [7] J. Feng, B. L. Su, H. Xia, S. Zhao, C. Gao, L. Wang, O. Ogbeide, J. Feng, T. Hasan, *Chem. Soc. Rev.* **2021**, *50*, 3842.
- [8] G. Hu, L. Yang, Z. Yang, Y. Wang, X. Jin, J. Dai, Q. Wu, S. Liu, X. Zhu, X. Wang, T.-C. Wu, R. C. T. Howe, T. Albrow-Owen, L. W. T. Ng, Q. Yang, L. G. Occhipinti, R. I. Woodward, E. J. R. Kelleher, Z. Sun, X. Huang, M. Zhang, C. D. Bain, T. Hasan, *Sci. Adv.* **2020**, *6*, 5029.
- [9] Y. Liu, J. Parisi, X. Sun, Y. Lei, *J. Mater. Chem. A* **2014**, *2*, 9919.
- [10] Z. Li, H. Li, Z. Wu, M. Wang, J. Luo, H. Torun, P. Hu, C. Yang, M. Grundmann, X. Liu, Y. Fu, *Mater. Horiz.* **2019**, *6*, 470.
- [11] J. Wang, H. Shen, Y. Xia, S. Komarneni, *Ceram. Int.* **2021**, *47*, 7353.
- [12] N. Ha, K. Xu, G. Ren, A. Mitchell, J. Z. Ou, *Adv. Intell. Syst.* **2020**, *2*, 2000063.
- [13] S. Kanaparathi, S. G. Singh, *Sens. Actuators, B* **2021**, *348*, 130725.
- [14] M. Drobek, J.-H. Kim, M. Bechelany, C. Vallicari, A. Julbe, S. S. Kim, *ACS Appl. Mater. Interfaces* **2016**, *8*, 8323.
- [15] T. Zhou, W. Dong, Y. Qiu, S. Chen, X. Wang, C. Xie, D. Zeng, *ACS Appl. Mater. Interfaces* **2021**, *13*, 54589.
- [16] O. Lupan, N. Ababii, D. Santos-Carballal, M.-I. Terasa, N. Magariu, D. Zappa, E. Comini, T. Pauporté, L. Siebert, F. Faupel, A. Vahl, S. Hansen, N. H. de Leeuw, *Nano Energy* **2021**, *88*, 106241.
- [17] S.-Y. Cho, H.-J. Koh, H.-W. Yoo, H.-T. Jung, *Chem. Mater.* **2017**, *29*, 7197.
- [18] V. V. Krivetskiy, M. D. Andreev, A. O. Efitorov, A. M. Gaskov, *Sens. Actuators, B* **2021**, *329*, 129187.
- [19] G. Bae, M. Kim, W. Song, S. Myung, S. S. Lee, K. S. An, *ACS Omega* **2021**, *6*, 23155.
- [20] T. C. Wu, J. Dai, G. Hu, W. B. Yu, O. Ogbeide, A. De Luca, X. Huang, B. L. Su, Y. Li, F. Udrea, T. Hasan, *Sens. Actuators, B* **2020**, *321*, 128446.
- [21] M. A. Akbar, A. A. Si Ali, A. Amira, F. Bensaali, M. Benammar, M. Hassan, A. Bermak, *IEEE Sens. J.* **2016**, *16*, 5734.
- [22] F. Schedin, A. K. Geim, S. V. Morozov, E. W. Hill, P. Blake, M. I. Katsnelson, K. S. Novoselov, *Nat. Mater.* **2007**, *6*, 652.
- [23] J. Hou, Y. Sun, Y. Wu, S. Cao, L. Sun, *Adv. Funct. Mater.* **2018**, *28*, 1704447.
- [24] N. Mohanty, A. Nagaraja, J. Armesto, V. H.-T. Berry, *Small* **2010**, *6*, 226.
- [25] S. Mo, Q. Zhang, S. Li, Q. Ren, M. Zhang, Y. Xue, R. Peng, H. Xiao, Y. Chen, D. Ye, *ChemCatChem* **2018**, *10*, 3012.
- [26] W. Wang, Q. Zhou, X. Fei, Y. He, P. Zhang, G. Zhang, L. Peng, W. Xie, *CrystEngComm* **2010**, *12*, 2232.
- [27] X. Ji, S. Cheng, L. Yang, Y. Jiang, Z.-J. Jiang, C. Yang, H. Zhang, M. Liu, *Nano Energy* **2015**, *11*, 736.
- [28] B. Urasinska-Wojcik, J. W. Gardner, *IEEE Sens. J.* **2018**, *18*, 3502.
- [29] T. Zhou, T. Zhang, J. Deng, R. Zhang, Z. Lou, L. Wang, *Sens. Actuators, B* **2017**, *242*, 369.
- [30] R. Roy, R. Thapa, S. Chakrabarty, A. Jha, P. Midya, E. M. Umar, K. Chattopadhyay, *Chem. Phys. Lett.* **2017**, *677*, 80.
- [31] *The IUPAC Compendium of Chemical Terminology* (Ed: V. Gold), International Union of Pure and Applied Chemistry (IUPAC), Research Triangle Park, NC **2019**.
- [32] T. Pham, G. Li, E. Bekyarova, M. E. Itkis, A. Mulchandani, *ACS Nano* **2019**, *13*, 3196.
- [33] E. C. Nallon, V. P. Schnee, C. Bright, M. P. Polcha, Q. Li, *ACS Sens.* **2016**, *1*, 26.
- [34] H. G. Moon, Y. Jung, S. D. Han, Y. S. Shim, B. Shin, T. Lee, J. S. Kim, S. Lee, S. C. Jun, H. H. Park, C. Kim, C. Y. Kang, *ACS Appl. Mater. Interfaces* **2016**, *8*, 20969.
- [35] J. Wei, X. Chu, X.-Y. Sun, K. Xu, H.-X. Deng, J. Chen, Z. Wei, M. Lei, *InfoMat* **2019**, *1*, 338.
- [36] K. Brown, S. Brittman, N. Maccaferri, D. Jariwala, U. Celano, *Nano Lett.* **2020**, *20*, 2.
- [37] K. Butler, D. Davies, H. Cartwright, O. Isayev, A. Walsh, *Nature* **2018**, *559*, 547.
- [38] R. Prajesh, V. Goyal, V. Saini, J. Bhargava, A. Sharma, A. Agarwal, *Mater. Res. Express* **2018**, *5*, 9.
- [39] K. Hassan, T. T. Tung, P. L. Yap, H. Rastin, N. Stanley, M. J. Nine, D. Losic, *ACS Sens.* **2021**, *6*, 3685.
- [40] D. D. Le, T. N. N. Nguyen, D. C. T. Doan, T. M. D. Dang, M. C. Dang, *Adv. Nat. Sci.: Nanosci. Nanotechnol.* **2016**, *7*, 9.